

# Unravelling the glue and the competing order in superconducting cuprates

S. Caprara<sup>1</sup>, C. Di Castro<sup>1</sup>, B. Muschler<sup>2</sup>, R. Hackl<sup>2</sup>, M. Lambacher<sup>2</sup>, A. Erb<sup>2</sup>, S. Komiya<sup>3</sup>, Y. Ando<sup>4</sup>, and M. Grilli<sup>1</sup>

<sup>1</sup> *CNR-INFN-SMC, and Dipartimento di Fisica, Università di Roma “La Sapienza”, P.le Aldo Moro 5, 00185 Roma, Italy*

<sup>2</sup> *Walther Meissner Institut, Bayerische Akademie der Wissenschaften, 85748 Garching, Germany*

<sup>3</sup> *Central Research Institute of the Electric Power Industry, Komae, Tokyo 201-8511, Japan and*

<sup>4</sup> *Institute of Scientific and Industrial Research, Osaka University, Ibaraki, Osaka 567-0047, Japan*

(Dated: November 22, 2018)

We present Raman scattering experiments in  $\text{La}_{2-x}\text{Sr}_x\text{CuO}_4$  single crystals at various doping levels  $x$  and compare the results with theoretical predictions obtained assuming an interaction mediated by spin and charge fluctuations. The light-scattering selection rules allow us to disentangle their respective contributions. We find that the glue spectral function is spin-dominated at low doping while the contribution of charge fluctuations becomes dominant around optimal doping. This indicates that the fluctuations of a nearly ordered state with coexisting spin and charge order support the superconducting pairing.

PACS numbers: 74.72.-h, 78.30.-j, 74.20.Mn, 71.45.Lr

## I. INTRODUCTION

Several systems, ranging from heavy fermions to manganites, from high-temperature superconducting cuprates to ruthenates, display anomalies in the metallic phase, with the violation of the well established paradigm of Fermi-liquid theory. As a matter of fact all these systems are characterized by strong electron-electron correlations and display similar phase diagrams, where an ordered phase is adjacent to the metallic state, possibly with the occurrence of superconductivity. This raises the question about the effective electron-electron interactions determining the metallic anomalies and possibly (high-temperature) superconductivity. In this respect cuprates are a paradigmatic example: Around optimal doping (where the superconducting critical temperature  $T_c$  is highest) these systems display anomalies in spectroscopic, transport, and thermodynamic properties. These anomalies should stem from the same effective interactions which also provide pairing. Understanding their nature is the hotly debated “glue issue”. For some people<sup>1-3</sup> the glue consists of strong, essentially instantaneous, electron-electron interactions, arising from the doped Mott insulator character of these systems. According to a second point of view, the low-energy effective interaction is due to a retarded bosonic-like glue<sup>4,5</sup>. Besides the standard phonons, spin waves<sup>6</sup> are the most quoted candidates, as reminiscent of the antiferromagnetism suppressed by doping. Quite naturally, the bosonic excitations might also be related to an elusive electronic order, which competes with superconductivity and should occur in underdoped cuprates (i.e. at doping less than optimal) either as a long-range ordered phase or in the form of local/dynamical short-range fluctuations<sup>7-14</sup>. The proximity to the corresponding “critical region” naturally brings along abundant critical fluctuations and leads to strongly momentum-, temperature- and doping-dependent bosonic effective interactions. Within this second point of view the identification of the glue also sheds light on the underlying

competing instability.

Here we show that exploiting the specific properties of Raman spectra in the different symmetry channels, fluctuations with different characteristic wavevectors can be identified. This is a quite general result for effective interactions that are strongly peaked at a finite wavevector (see Appendix for technical details) and it might render Raman spectroscopy a particularly powerful tool to detect and study elusive orders occurring at finite wavevectors. More specifically, here we start from a phenomenology for spin and charge fluctuations, predict the Raman spectra in the two  $B_{1g}$  and  $B_{2g}$  symmetry channels and compare our theoretical results with experimental results on  $\text{La}_{2-x}\text{Sr}_x\text{CuO}_4$  (LSCO) samples at various doping levels  $x$  and temperatures  $T$ . In this way we disentangle the contribution of spin and charge fluctuations, which can be identified as the relevant bosonic modes in these systems. This identification, not only clarifies the glue issue, but also strongly indicates a nearly spin/charge-ordered state as the competing phase in underdoped cuprates, which evolves from a dominating spin order at low doping, near the Mott insulator, to a charge-dominated order on the overdoped side.

## II. EXPERIMENTAL DETAILS

The samples were grown using the traveling solvent floating zone (TSFZ) method. The characterization is presented in Table I.

The lowest doping was  $x = 0.15$  close to the  $T_c$  maximum where Landau-Fermi liquid theory should still be applicable. The overdoped sample with  $x = 0.26$  had no indication of superconductivity above 2K. All samples were post-annealed in pure oxygen at 1 bar to improve the crystal quality. The spectra were taken on polished surfaces. In the case of  $\text{La}_{1.74}\text{Sr}_{0.26}\text{CuO}_4$  the results were

TABLE I: List of samples. Samples labeled with *a* have been prepared by M. Lambacher and A. Erb (WMI Garching)<sup>50</sup>, *b* by Seiki Komiya and Yoichi Ando (CRIEPI, Tokyo and Osaka University) and *c* by N. Kikugawa and T. Fujita (Hiroshima and Tokyo). The transition temperatures were measured either resistively or via magnetometry or via the non-linear ac response.

sample	doping <i>x</i>	$T_c$ (K)	$\Delta T_c$ (K)	comment
La <sub>1.85</sub> Sr <sub>0.15</sub> CuO <sub>4</sub>	0.15	38	3	O <sub>2</sub> annealed <i>a</i>
La <sub>1.83</sub> Sr <sub>0.17</sub> CuO <sub>4</sub>	0.17	39	1	O <sub>2</sub> annealed <i>b</i>
La <sub>1.80</sub> Sr <sub>0.20</sub> CuO <sub>4</sub>	0.20	24	3	O <sub>2</sub> annealed <i>a</i>
La <sub>1.75</sub> Sr <sub>0.25</sub> CuO <sub>4</sub>	0.25	12	3	O <sub>2</sub> annealed <i>a</i>
La <sub>1.74</sub> Sr <sub>0.26</sub> CuO <sub>4</sub>	0.26	0	-	O <sub>2</sub> annealed <i>c</i>

compared to those from a cleaved surface and were found to be identical to within the experimental error<sup>49</sup>.

The Raman experiments were performed with standard equipment. For excitation an Ar ion laser operated at 458 nm was used. The angle of incidence of the incoming photons was 66°. The polarization state outside was prepared in a way that photons inside the sample had the desired state. Scattered light of a selected polarization was collected along the surface normal and focused on the entrance slit of the spectrometer. The energy-selected photons were detected with a liquid nitrogen cooled CCD detector. All spectra are corrected for the sensitivity of the complete setup. We generally show the imaginary part of response functions,  $\chi''_\mu$ , at pure symmetries  $\mu = B_{1g}, B_{2g}$  which are related to the measured cross section as

$$\frac{d^2\sigma_\mu}{d\tilde{\Omega}d\omega_s} = A \frac{\omega_i}{\omega_s} \{1 + n(\omega, T)\} \chi''_\mu(\mathbf{q} = 0, \omega, T) \quad (1)$$

with  $\sigma_\mu$  the photon cross section in symmetry  $\mu$ ,  $\tilde{\Omega}$  the solid angle accepted by the collection optics  $\omega = \omega_i - \omega_s$  the energy transferred to the system,  $A$  a constant absorbing all factors to convert  $\chi''_\mu$  into a cross section and  $n(\omega, T) = [\exp(\omega/T) - 1]^{-1}$  the Bose-Einstein factor. To simplify the notation we drop hereafter the index  $\mu$ , since the formal expressions in the following are the same for all symmetry channels.

### III. RAMAN SPECTRA

Electronic Raman scattering is a bulk (nearly surface-insensitive) probe and it measures a response function  $\chi''(\omega, T)$  analogous to that of the optical conductivity<sup>15</sup>. However, while the latter yields an average over the entire Brillouin zone, light scattering projects different parts of the Brillouin zone for different polarizations of the incoming and outgoing photons<sup>16</sup>, thereby introducing specific form factors in  $\chi''(\omega, T)$ . We consider Raman spectra in the  $B_{1g}$  and  $B_{2g}$  channels obtained from the systematic analysis of several LSCO samples at different doping levels  $x$  ranging from the nearly optimal up to the strongly

overdoped region (see Fig. 1). Generally we observe that the overall shape of the spectra in  $B_{1g}$  and  $B_{2g}$  channels is quite different up to 3000-4000  $\text{cm}^{-1}$ , while at higher frequency the two spectra have similar shape and intensity. At frequencies up to 2000  $\text{cm}^{-1}$ , the  $B_{1g}$  spectra can be schematized by a hump appearing as a shoulder of a slightly larger hump peaked at  $\omega \sim 4000 \text{ cm}^{-1}$ . On the other hand,  $B_{2g}$  spectra display a plateau up to about 1000  $\text{cm}^{-1}$ . At higher frequencies the absorption rises and a hump nearly twice as large, similar to the one found in  $B_{1g}$ , appears at about 4000  $\text{cm}^{-1}$ . The temperature dependence of the spectra is altogether weak (see Fig. 2a), but it may even be opposite in the two channels in an intermediate frequency range. In particular the temperature dependence of the  $B_{2g}$  spectra corresponds to those of the optical conductivity for  $x > 0.05$ . In  $B_{1g}$  symmetry at low-intermediate dopings there is a strong extra contribution from fluctuations at low frequency<sup>43,44,49</sup>. Therefore we confine the analysis to  $x \geq 0.15$ .

A first remark is now in order: Although the Raman form factors select different regions of the Brillouin zone, and therefore explore different electronic structures, it is rather unlikely that the changes in doping and temperature in the two channels [see the low-energy part of Figs. 2(a) and the overall shapes of the responses in Figs. 1(b-e)] can simply be attributed to diverse evolutions of the underlying fermionic band structures. Also a scattering mechanisms with zero characteristic momentum<sup>3,8,9</sup>, would act in the same way in the two channels hardly explaining their different behaviours. Guided by a wealth of experimental evidences for a prominent tendency of LSCO cuprates to form charge-ordered states (stripes or checkerboard), we show below that different shapes (and different temperature and doping evolutions) of the spectra in the two channels naturally arise from quasiparticles (QPs) coupled to distinct charge and spin fluctuations, each one having its own dynamics and characteristic wavevector.

### IV. THE “GLUE” COLLECTIVE MODES

Here we approach the identification of the glue extracting its properties from the Raman data. We start from a form of damped glue boson collective modes (CMs), which is customary for spin fluctuations<sup>6,17</sup>

$$D_\lambda(\mathbf{q}, \omega) = -\frac{1}{m_\lambda + \nu_\lambda(\mathbf{q} - \mathbf{q}_\lambda)^2 - i\omega - \omega^2/\tilde{\Omega}_\lambda} \quad (2)$$

where  $\lambda = c, s$  refers to charge or spin CMs substantially peaked at characteristic wavevectors  $\mathbf{q}_s \approx (\pi, \pi)$  and  $\mathbf{q}_c \approx (\pm\pi/2, 0), (0, \pm\pi/2)$  respectively. Here the mass  $m_\lambda$  is the minimum energy required to excite the CM and  $\nu_\lambda$  is a fermion scale setting the CM momentum dispersion. This dispersion is limited by an energy cutoff  $\Lambda_\lambda$ . The dimensionless quantities  $m_\lambda/\Lambda_\lambda$  are the inverse square correlation lengths (in units of the lattice spacing), which measure the typical size of ordered domains.

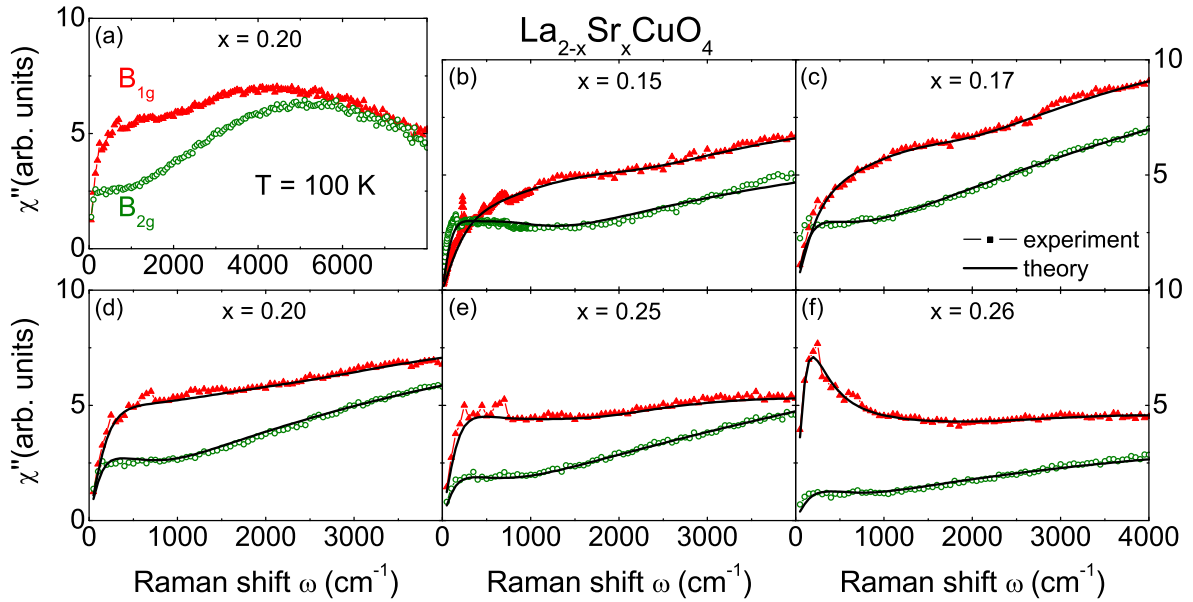


FIG. 1: (a) Experimental Raman response  $\chi''_{\mu}(\omega, T)$  of LSCO at  $x = 0.20$  on a broad frequency range up to  $8000 \text{ cm}^{-1}$  at intermediate  $T = 104 \text{ K}$  in the  $B_{1g}$  channel (green circles) and in the  $B_{2g}$  channel (red triangles). (b-e) Raman response  $\chi''_{\mu}(\omega, T)$  of LSCO at  $x = 0.15, 0.17, 0.20, 0.25,$  and  $0.26$  on a reduced frequency range up to  $4000 \text{ cm}^{-1}$ . Data in the  $B_{1g}$  channel are given by green circles, while the spectra in the  $B_{2g}$  symmetry are given by red triangles. The various spectra are taken at similar temperatures around  $T \approx 100 \text{ K}$ . The results of the fits obtained within the “nearly-critical” charge/spin theory (see text) are given by the black solid lines.

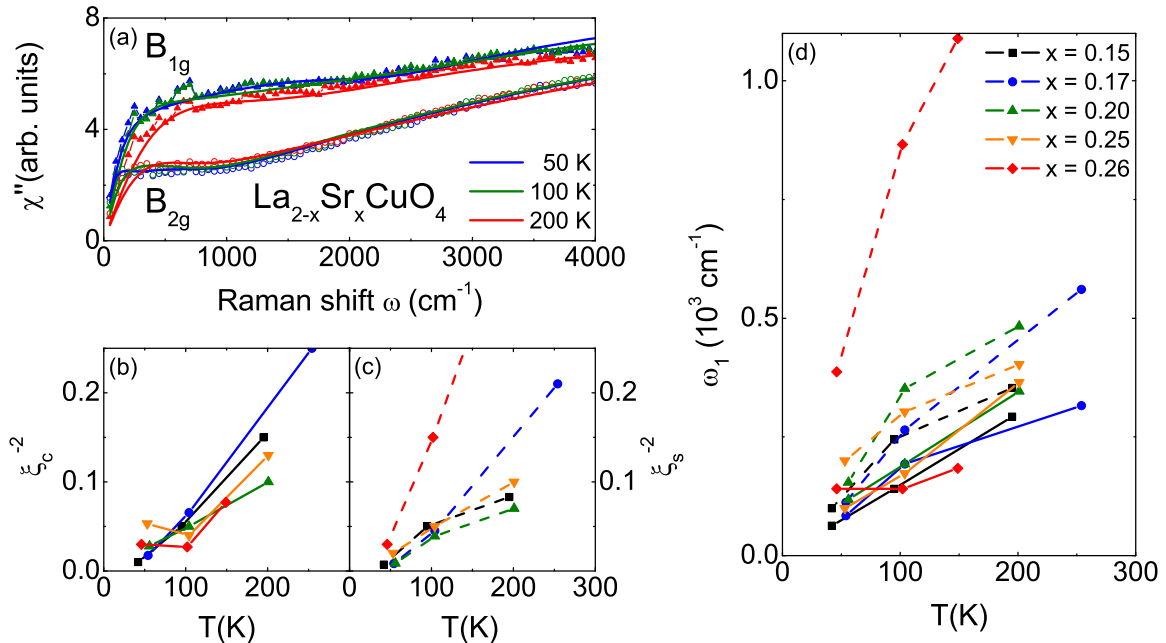


FIG. 2: (a) Raman response  $\chi''_{\mu}(\omega, T)$  of LSCO at  $x = 0.20$  in the  $B_{1g}$  (circles) and  $B_{2g}$  (triangles) at three different temperatures above  $T_c$  and the related fits (solid curves) obtained within the nearly critical scheme described in the text:  $T = 56 \text{ K}$  (blue circles and curve),  $T = 104 \text{ K}$  (green circles and curve),  $T = 201 \text{ K}$  (red circles and curve). (b) Temperature dependence of the inverse square correlation length  $\xi_c^{-2}$  of the charge modes at different dopings ( $x = 0.15$  blue,  $x = 0.17$  red,  $x = 20$  green,  $x = 0.25$  black). (c) Same as in (b) for the inverse square correlation length  $\xi_s^{-2}$  of the spin collective modes. (d) Temperature dependence of the low-frequency typical energy scale  $\omega_1 = \sqrt{m\Omega}$  of the charge and spin collective modes.

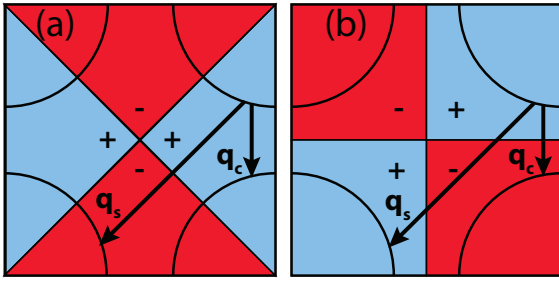


FIG. 3: Hot spot structure for both charge (with  $\mathbf{q}_c$ ) and spin (with  $\mathbf{q}_s$ ) scattering. In panels (a) and (b) the sign structures of the form factors for the  $B_{1g}$  and  $B_{2g}$  channels,  $\gamma_{1g}(\mathbf{k}) = \cos(k_x) - \cos(k_y)$  and  $\gamma_{2g}(\mathbf{k}) = \sin(k_x)\sin(k_y)$  (we use a unit lattice spacing), respectively, are reported.

The  $i\omega$  term establishes the low-energy diffusive character of these fluctuations due to decay into particle-hole pairs, whereas above the scale set by  $\bar{\Omega}_\lambda$  the CM has a more propagating character.

The CMs mediate strongly momentum-dependent scattering between the QPs. At low energy this scattering mechanism is more effective for QPs on the Fermi surface, which are connected by the characteristic CM momenta (the so-called “hot spots”). For the typical  $\mathbf{q}_s$  and  $\mathbf{q}_c$  in the cuprates the hot spots for spin and charge CMs occur in the same regions of the Fermi surface near the  $(\pm\pi, 0)$  and  $(0, \pm\pi)$  points of the Brillouin zone (see Fig. 3).

The Raman response function can be expressed in terms of a memory function as

$$\chi(\omega) = \frac{\chi_0\omega}{\omega + M(\omega)}. \quad (3)$$

Here  $\chi_0$  is the purely real low-frequency Raman response function in the absence of any scattering process. As in standard approaches<sup>18,19</sup>, our perturbative memory function calculation is limited to processes which involve the exchange of one CM ( $\lambda = c$  or  $s$ ). The specific form of the fluctuations (2) allows one to identify and analytically calculate the dominant contribution to  $M = M_c + M_s$  (for details see the Appendix) yielding for the imaginary part

$$\begin{aligned} \text{Im}M_\lambda(\omega) = & \frac{1}{\omega} \int_0^\infty dz [\alpha^2 F_\lambda(z)] \left[ 2\omega \coth\left(\frac{z}{2T}\right) \right. \\ & \left. - (z + \omega) \coth\left(\frac{z + \omega}{2T}\right) + (z - \omega) \coth\left(\frac{z - \omega}{2T}\right) \right] \end{aligned} \quad (4)$$

which has the meaning of a frequency-dependent inverse scattering time. The crucial physical ingredient in Eq. (4) is the spectral distribution  $\alpha^2 F$  appearing, e.g., in the textbook Eliashberg theory of superconductivity (the so-called “glue function”), which in our case reads

$$\begin{aligned} \alpha^2 F_\lambda(\omega) = & g_\lambda \left[ \arctan\left(\frac{\Lambda_\lambda \bar{\Omega}_\lambda - \omega^2}{\bar{\Omega}_\lambda \omega}\right) \right. \\ & \left. - \arctan\left(\frac{m_\lambda \bar{\Omega}_\lambda - \omega^2}{\bar{\Omega}_\lambda \omega}\right) \right] \end{aligned} \quad (5)$$

The dimensionless parameter  $g_\lambda$ , which also absorbs  $\nu_\lambda$ , describes the coupling between CMs and QPs. This spectrum is roughly contained in the range between  $\omega_1 \approx \sqrt{\bar{\Omega}m}$  and  $\omega_2 \approx \sqrt{\bar{\Omega}\Lambda}$ . When  $\bar{\Omega}$  is large,  $\alpha^2 F(\omega)$  has the broadly peaked shape of a glue function due to diffusive CMs. For small  $\bar{\Omega}$ , i.e., for rather propagating CMs,  $\alpha^2 F(\omega)$  has a “flattish” box-like shape. This latter form of the scattering spectrum has been phenomenologically assumed since the early days of high- $T_c$  superconductivity by the marginal-Fermi-liquid theory<sup>20,21</sup>. We find it non trivial that the marginal Fermi liquid phenomenology in momentum-integrated quantities (tunnelling spectra, optics, Raman, etc.) is obtained here from a microscopic strongly momentum dependent scattering mechanism. When adapted to the calculation of optical conductivity, our formalism contains as limiting cases the marginal-Fermi liquid and the diffusive CM considered in Ref. 22 and reproduces their results.

Our first general result is that the different experimental spectra in the  $B_{1g}$  and  $B_{2g}$  channels are obtained and correspond to a more diffusive and a more propagating CM respectively (an extended presentation of this generic result is given in the Appendix).

## V. ANALYSIS OF THE COLLECTIVE MODE SPECTRA

Despite the fact that both charge and spin CMs couple to the QPs in the same hot-spot regions of the Brillouin zone, symmetry arguments imply that their different characteristic wavevectors gives rise to important cancellations in the memory function depending on the channel form factors. The cancellation occurs when the relevant scattering wavevectors connect regions where the form factors have the same sign (see Eq. (A1) in the Appendix). Conversely the largest contribution is obtained when the critical wavevectors connect regions with opposite sign of the form factors. Inspection of Fig. 3 shows that the spin CM dominates the  $B_{1g}$  spectra, while the charge CM dominates the spectra in the  $B_{2g}$  channel. These “selection rules” are effective at low frequency and gradually fail upon increasing the energy of the Raman scattering. This failure is effectively taken into account by a gradual frequency-dependent switching on (from about  $1000 \text{ cm}^{-1}$ ) of the coupling between the QPs and the “forbidden” CM in each channel (for details see Appendix). We do not attempt to fit the data above  $4000 \text{ cm}^{-1}$  because multiple scattering processes become important making the distinction between  $M_c$  and  $M_s$  meaningless. At this point the spectra eventually become similar in shape [see Fig. 1(a)].

Adjusting the CM parameters and their coupling to the QPs we fit the experimental spectra (see Fig. 1). Remarkably, the different shapes and doping evolutions can be tracked. For instance, the  $B_{1g}$  spectrum evolves from the rounded shape (characteristic of a strong scattering already at low energies) at  $x = 0.15$  to the narrow peak typical of a weakly scattered “Drude-like” be-

haviour at  $x = 0.26$ . From these systematic fits we extract the corresponding evolution of the glue functions (see Fig. 4) and of the related CMs [see Fig. 2(b-d)]. Quite naturally in the substantially doped regime we are considering, we find that the spin spectra (dashed lines) have a marked diffusive character (typical values of  $\bar{\Omega}$  are in the range of  $1000 - 3000 \text{ cm}^{-1}$ ). The overall weight  $W_s$  of the glue functions due to spin exchange [see the dashed lines in Fig. 4(f)] is still rather large at  $x = 0.17$ , but then decreases and becomes very small in the most overdoped sample ( $x = 0.26$ ) in agreement with inelastic neutron scattering data<sup>23,24</sup>. Conversely, the shape of the charge-mediated glue is more propagating-like (roughly resembling the shape proper to a marginal-Fermi-liquid glue) because the typical  $\bar{\Omega} \sim 200 \text{ cm}^{-1}$  is much lower than in the spin case. Thus, the charge-mediated glue function is centered at typical phonon frequencies of the cuprates. This agrees well with the idea that charge-ordering in cuprates is phonon-driven<sup>7</sup>, with a strong mixing between the electronic and the lattice degrees of freedom<sup>25</sup>. Charge CMs have a marked phononic character at generic  $\mathbf{q}$  and acquire a strong electronic component at  $\mathbf{q} \sim \mathbf{q}_c$ , where this composite excitation has an anomalous softening with weight displacement down to low energies of order  $m_c$ . This behaviour is reflected in the temperature dependence of the charge glue functions, which, while having their centre at about  $500 \text{ cm}^{-1}$ , also have a substantial spectral density at low energy when temperature is low.

The overall weight of the charge glue  $W_c$  evolves in the opposite way with respect to the spin weight. It is relatively small at  $x = 0.15$ , increases reaching a maximum at  $x = 0.20 - 0.25$  and then slightly decreases at  $x = 0.26$  [see Fig. 4(f)]. Of course this doping evolution should be reflected in the doping evolution of the superconducting critical temperature. Owing to the strongly retarded character of the interaction, a full Eliashberg analysis of superconducting properties is required.

Both charge and spin CMs have strongly temperature dependent inverse square correlation lengths  $\xi^{-2} = m/\Lambda$  (see Figs. 2(b),(c)) which only affect the low-frequency part of the glue functions, but have a marked influence on the Raman spectra over the whole frequency range. Without this temperature dependence (like, e.g., for standard phonon scattering), the spectra would be much more temperature dependent, due to the bosonic occupation factors in Eq. (4).

In general, we find that the observed temperature dependence of the charge inverse square correlation length  $\xi_c^{-2}$  is in qualitative agreement with an underlying critical behaviour related to a competing charge-ordering instability. In particular, we notice that the linear temperature dependence at  $x = 0.20$  extrapolates to zero at  $T \rightarrow 0$  indicating that this doping is quite close to the value of the quantum critical point usually reported to be at  $x = 0.19$ <sup>10,26</sup>).

We also find that the spin correlation length is of the same order as the correlation of the charge ordering at

low  $T$ , consistent with the idea that spin fluctuations can survive at high doping, far from the antiferromagnetic region, if sustained and “enslaved” by charge-depleted fluctuating regions. This connection is also apparent in Fig. 2(d), where a similar energy scale  $\omega_1$  for charge and spin is reported. This shows that the “bulk” of the spectrum for the two collective degrees of freedom has essentially the same energy threshold.

## VI. OTHER EXPERIMENTS

Coupling functions derived recently from the Raman spectra in one Bi2212 sample yield differences in the two symmetries, with a prominent spin scattering in the  $B_{1g}$  channel<sup>27</sup>. However, the identification of spin and charge modes and the assessment of their contribution to the two channels at low frequency has been made possible by the procedure described here. The present work may solve the long-standing puzzle in the cuprates regarding the relevance of the spin vs. phononic scattering mechanism affecting, e.g., the electron dispersion and giving rise to the kinks in ARPES spectra<sup>6,28,29</sup>: both spin and mixed charge-phonon modes contribute to the anomalies of the electronic dispersion because both modes share the same hot-spot region and have a substantial weight. It is also encouraging that recent ARPES<sup>30</sup> and STM<sup>31-33</sup> experiments support the role of charge-order scattering in electronic spectra. Moreover, the relevance of charge-order excitations with a marked phononic character, can also provide a rationale for various isotopic effects detected along the years in cuprates<sup>34-38</sup>.

The simultaneous presence of two CMs dressing the QPs, was also recently found in optical spectroscopy on Bi 2201 and Bi 2212 samples<sup>39,40</sup>. One could also similarly interpret the  $\alpha^2F$  recently obtained from ARPES spectra<sup>41,42</sup>. These findings are in agreement with our analysis, because in optical conductivity and in ARPES the channel-dependent form factors are absent and both CMs contribute. As a result we simply need to add the spin and charge glue-functions to reproduce the experiments. Although we did not attempt a precise fitting and comparison with the experimental data, we explain why the optical scattering time ( $Im M^{opt}(\omega)$ ) above  $1000 \text{ cm}^{-1}$  displays a very weak (if not absent) temperature dependence in underdoped samples, which gradually increases upon doping (see Fig. 5(a)-(c))<sup>45-47</sup>. This behaviour simply arises from the temperature dependence of the CM masses (both charge and spin): upon increasing  $T$ , the masses grow producing a less marked increase of the scattering. This compensation is less effective upon increasing doping.

While the above spectroscopies indirectly probe the CM through their effects of the QPs, other spectroscopies directly probing the charge or spin CMs provide pictures consistent with our findings. Concerning the spin modes, there is a correspondence between our spin glue functions and the spin spectral functions obtained from inelastic neutron scattering. Specifically we found that above

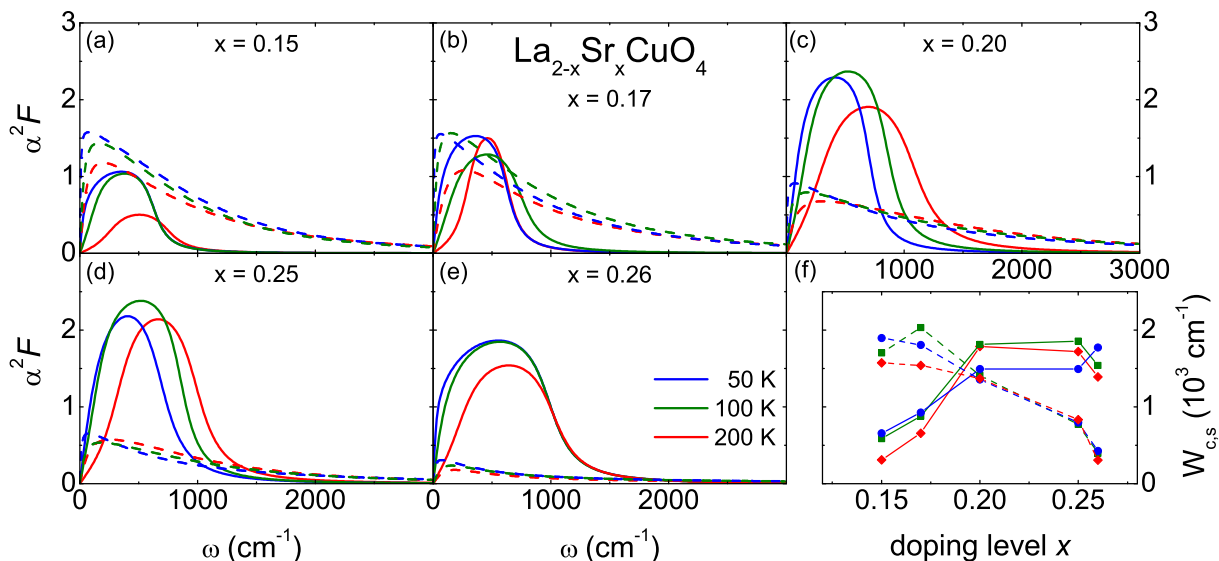


FIG. 4: (a)-(e) Glue functions due to the “allowed” modes in the fitted spectra of Fig. 1. The solid lines are the glue functions due to charge CM, while the dashed lines are the spin CM glue functions. Blue, green and red curves refer to low ( $T \sim 50$  K), intermediate ( $T \sim 100$  K), and high ( $T \sim 150 - 200$  K) respectively. (a)  $x = 0.15$ ,  $T = 42$  K, 95 K, and 195 K; (b)  $x = 0.17$ ,  $T = 54$  K, 104 K, 254 K; (c)  $x = 0.20$ ,  $T = 56$  K, 104 K, 201 K; (d)  $x = 0.25$ ,  $T = 53$  K, 104 K, 201 K; (e)  $x = 0.26$ ,  $T = 46$  K, 102 K, 149 K; (f) Total weight of the glue functions mediated by charge  $W_c$  (solid lines) and spin  $W_s$  (dashed lines) as a function of doping  $x$

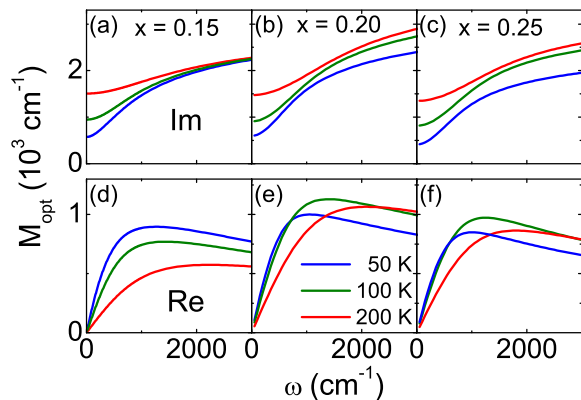


FIG. 5: Imaginary (a-c) and real (d-f) parts of the optical memory functions obtained summing the charge and the spin glue functions reported in Fig. 4. The correspondence between colors and temperatures is the same as in Fig. 4. For details of the calculations see the Appendix

$x = 0.20$  the spin excitation intensity rapidly decreases, by about a factor one half between  $x = 0.25$  and  $x = 0.26$ . This corresponds well to the spin suppression observed in Refs. 23,24. Dynamical charge fluctuations are less accessible. However, we interpreted previous results of Raman absorption in underdoped LSCO samples at low frequencies (up to a few hundreds of wavenumbers)<sup>43</sup> in terms of direct excitations of two charge CMs<sup>44</sup>. Remarkably the values and the temperature dependencies of  $m_c(T)$

obtained at such low frequencies and in much less doped samples, and from different excitation processes, are in close agreement with the behaviour of  $m_c(T)$  found in the presently analyzed optimally and overdoped samples.

## VII. SUMMARY AND PERSPECTIVES

In this paper we demonstrate that a retarded bosonic glue accounts well for the rich variety of shapes, and of doping and temperature dependencies of Raman spectra in LSCO. We show that, fully exploiting the interplay between the sign of the Raman form factors and the peaked momentum structure of the fluctuations, the dominant absorption in the  $B_{1g}$  and  $B_{2g}$  channels at low energy mostly arises from QPs scattering either with spin or charge CMs respectively. The different shapes of the Raman spectra in  $B_{1g}$  and  $B_{2g}$  symmetry is the result of the more diffusive or propagating character of the corresponding dominant CMs. The more propagating charge CM corresponds to a rather flattish glue function thereby reproducing the phenomenology of marginal-Fermi-liquid theory in momentum integrated responses.

Our main result is a complete description of doping and temperature evolution of the glue functions due to charge and spin CMs. The relative importance of the two scattering mechanisms switches from spin to charge by increasing doping. While the relevance of dynamical spin scattering was already inferred both from theoret-

ical approaches<sup>5</sup> and phenomenological analyses<sup>48</sup>, the simultaneous presence of mixed phonon-charge-density fluctuations and their increasing relevance with doping is assessed here for the first time. Moreover, the relevance of charge fluctuations also indicates that a nearly charge-ordered phase competes with superconductivity in underdoped LSCO. Our analysis opens the way to the wide field of investigations based on a specific form of a retarded bosonic glue.

### Acknowledgments

We acknowledge discussions with C. Castellani, T. Devereaux, and J. Lorenzana. S.C., C. D.C., and M.G. acknowledge financial support from the MIUR-PRIN07 prot. 2007FW3MJX\_003. R.H. and B. M. acknowledge support from the DFG under grant-no. Ha2071/3 via Research Unit FOR538. M.L. and A.E. were supported in the same network under grant number Er342/1.

## Appendix A: Memory function

We outline here the main steps of the calculation of the memory function that appears in the Raman response equation (2). To simplify the notation we drop the index  $\mu$ , since the formal expressions are the same for all symmetry channels. Within a perturbative approach limited to the exchange of a single CM, the memory function reads

$$M = -\omega \frac{\chi_{SV}}{\chi_0},$$

where  $\chi_0$  is the purely real low-frequency Raman response function in the absence of any scattering process, and  $\chi_{SV}$  is the contribution due to CM selfenergy (S) and vertex (V) corrections (see Fig. 6). Here we are neglecting impurity scattering as well as sources of scattering other than CMs. The fermion loops entering the expression of  $\chi_{SV}(\Omega_M)$ , where  $\Omega_M$  is the external Matsubara frequency, are

$$\begin{aligned} S_1(\mathbf{q}, \omega_n, \Omega_M) &= -2T\tilde{g}^2 \sum_{\epsilon_\ell} \int \frac{d^2\mathbf{k}}{(2\pi)^2} \gamma_{\mathbf{k}}^2 \mathcal{G}(\mathbf{k}, \epsilon_\ell - \Omega_M) \\ &\quad \times \mathcal{G}(\mathbf{k}, \epsilon_\ell) \mathcal{G}(\mathbf{k} + \mathbf{q}, \epsilon_\ell + \omega_n) \mathcal{G}(\mathbf{k}, \epsilon_\ell), \\ S_2(\mathbf{q}, \omega_n, \Omega_M) &= -2T\tilde{g}^2 \sum_{\epsilon_\ell} \int \frac{d^2\mathbf{k}}{(2\pi)^2} \gamma_{\mathbf{k}}^2 \mathcal{G}(\mathbf{k}, \epsilon_\ell + \Omega_M) \\ &\quad \times \mathcal{G}(\mathbf{k}, \epsilon_\ell) \mathcal{G}(\mathbf{k} + \mathbf{q}, \epsilon_\ell + \omega_n) \mathcal{G}(\mathbf{k}, \epsilon_\ell), \\ V(\mathbf{q}, \omega_n, \Omega_M) &= -2T\tilde{g}^2 \sum_{\epsilon_\ell} \int \frac{d^2\mathbf{k}}{(2\pi)^2} \gamma_{\mathbf{k}} \gamma_{\mathbf{k}+\mathbf{q}} \mathcal{G}(\mathbf{k}, \epsilon_\ell) \\ &\quad \times \mathcal{G}(\mathbf{k}, \epsilon_\ell + \Omega_M) \mathcal{G}(\mathbf{k} + \mathbf{q}, \epsilon_\ell + \omega_n + \Omega_M) \\ &\quad \times \mathcal{G}(\mathbf{k} + \mathbf{q}, \epsilon_\ell + \omega_n), \end{aligned}$$

where  $\mathcal{G}(\mathbf{k}, \epsilon_\ell) = (i\epsilon_\ell - \xi_{\mathbf{k}})^{-1}$  is the Matsubara Green's function of free fermions with band dispersion  $\xi_{\mathbf{k}}$ . To calculate  $\chi_{SV}$ , we make now two main approximations. First, we notice that the CM propagator is peaked at a wavevector  $\mathbf{q} = \mathbf{q}_\lambda$ , whereas the fermion loops are

smooth functions of the integrated wavevector  $\mathbf{q}$ . Thus, in the integral over  $\mathbf{q}$  that appears in the expression for  $\chi_{SV}$ , the fermion loops can be factorized and evaluated at  $\mathbf{q} = \mathbf{q}_\lambda$ . Once this factorization is introduced, the integral over  $\mathbf{k}$  in the fermion loops is dominated by QPs near the hot spots (HS) at the Fermi surface associated with  $\mathbf{q}_\lambda$ . The two-dimensional integral over  $\mathbf{k}$  is then suitably transformed into an integral over the QP dispersions at the two hot spots connected by  $\mathbf{q}_\lambda$ ,  $\xi_{HS}$  and  $\xi'_{HS}$  (this approximation corresponds to a linearization of the band dispersion around the hot spots, see Ref.<sup>6</sup>). This change of variables involves the Jacobian of the transformation  $J$  evaluated at the hot spots, giving rise to a dimensionless prefactor  $\tilde{J} \equiv J\tilde{g}^2$ . The subsequent sum over the fermion Matsubara frequency  $\epsilon_\ell$  may be carried out explicitly.

In the forthcoming discussion, it is crucial to observe that the selfenergy contribution contains two Raman form factors evaluated at the same hot spot,  $\gamma^{HS}$ , whereas one of the two form factors appearing in the vertex contribution,  $\gamma^{HS'}$ , is evaluated at a different hot spot, connected to the former by  $\mathbf{q}_\lambda$ .

After evaluating the fermion loops, within the approximations outlined above, we obtain the contribution to the Raman response

$$\chi_{SV}(\Omega_M) = T \sum_{\omega_n} \Gamma_{SV}(\omega_n, \Omega_M) \int \frac{d^2\mathbf{q}}{(2\pi)^2} \mathcal{D}(\mathbf{q}, \omega_n),$$

where  $\mathcal{D}(\mathbf{q}, \omega_n) = -[m_\lambda + \nu_\lambda(\mathbf{q} - \mathbf{q}_\lambda)^2 + |\omega_n| + \omega_n^2/\tilde{\Omega}_\lambda]^{-1}$  is the Matsubara CM Green's function and the leading contribution of the fermion loops is fully included in the function  $\Gamma_{SV}(\omega_n, \Omega_M) \equiv [S_1(\mathbf{q}, \omega_n, \Omega_M) + S_2(\mathbf{q}, \omega_n, \Omega_M) + V(\mathbf{q}, \omega_n, \Omega_M)]_{\mathbf{q}=\mathbf{q}_\lambda}$ .

By explicit evaluation, following the procedure outlined above, we find

$$\Gamma_{SV}(\omega_n, \Omega_M) = 4\pi\tilde{J}\gamma^{HS} \left( \gamma^{HS'} - \gamma^{HS} \right) \frac{|\omega_n| - |\Omega_M|}{\Omega_M^2},$$

for  $-|\Omega_M| < \omega_n < |\Omega_M|$ , and  $\Gamma_{SV}(\omega_n, \Omega_M) = 0$  elsewhere. This expression enforces the selection rule quoted in the text: the main contribution to the fermion loops is non vanishing only if the Raman form factor  $\gamma_{\mathbf{k}}$  has a different sign on the two hot spots connected by  $\mathbf{q}_\lambda$ . For the characteristic wavevectors of spin and charge CMs, this occurs in the  $B_{1g}$  and  $B_{2g}$  symmetry channel, respectively.

After a shift of the origin of momentum space to  $\mathbf{q}_\lambda$ , the integral over  $\mathbf{q}$  becomes straightforward. The sum over the Matsubara frequencies  $\omega_n$  is then transformed into an integral over the real axis by standard techniques, exploiting the fact that the boson frequencies  $\omega_n$  are the simple poles of  $\coth(z/2T)$ . After causal continuation of the external Matsubara frequency  $\Omega_M$  to the real frequency  $\omega$ , we finally obtain the contribution to the Raman response function due to the QP scattering with

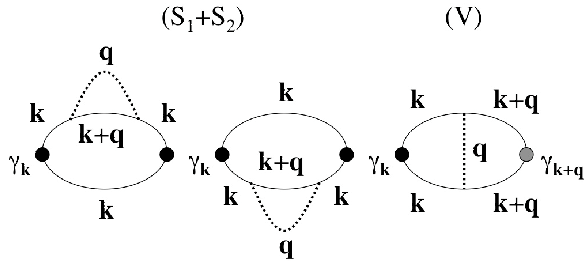


FIG. 6: Self-energy (S) and vertex (V) diagrams corrections to the Raman response function with the exchange of a single collective mode. The black dots represent the  $\gamma_{\mathbf{k}}$  form factor, while the shaded dot represents  $\gamma_{\mathbf{k}+\mathbf{q}}$ . The dotted lines represent collective mode Green's functions

CMs,

$$\begin{aligned} \chi_{SV}(\omega) = & -\frac{\tilde{J}\gamma^{HS}(\gamma^{HS} - \gamma^{HS'})}{2\pi\nu_{\lambda}\omega^2} P \int_{-\infty}^{+\infty} dz \\ & \times \left[ \frac{1}{2} \log \frac{\bar{\Omega}_{\lambda}^2 z^2 + (\bar{\Omega}_{\lambda}\Lambda_{\lambda} - z^2)^2}{\bar{\Omega}_{\lambda}^2 z^2 + (\bar{\Omega}_{\lambda}m_{\lambda} - z^2)^2} \right. \\ & \left. + i \left( \arctan \frac{\bar{\Omega}_{\lambda}\Lambda_{\lambda} - z^2}{\bar{\Omega}_{\lambda}z} - \arctan \frac{\bar{\Omega}_{\lambda}m_{\lambda} - z^2}{\bar{\Omega}_{\lambda}z} \right) \right] \\ & \times (\omega - z) \left( \coth \frac{z}{2T} - \coth \frac{z - \omega}{2T} \right), \end{aligned}$$

where the symbol  $P$  indicates that the principal part of the integral must be considered whenever a simple pole of the integrand is met on the real axis. Although this is not immediately evident, by changing the integration variable to  $-z$  and summing one half of each of the two expressions it may be easily shown that the imaginary part of the resulting memory function is an odd function of the external frequency  $\omega$ , as required by causality. This explicit antisymmetrization with respect to  $\omega$  yields the results for  $ImM$  and  $\alpha^2 F$  quoted in the text, with the dimensionless effective coupling

$$g_{\lambda} = \frac{\tilde{J}\gamma^{HS}(\gamma^{HS} - \gamma^{HS'})}{2\pi\nu_{\lambda}\chi_0}.$$

In the presence of multiple hot spots and/or multiple values of the characteristic wavevectors  $\mathbf{q}_{\lambda}$  (as implied, e.g., by the symmetry of the lattice), the overall dimensionless coupling is intended to be a sum over all the hot spots and  $\mathbf{q}_{\lambda}$ 's.

### Appendix B: Shape of the Raman response

The connection between the overall shape of the Raman response and the properties of the CMs is fully entailed in the form of the CM glue function  $\alpha^2 F(\omega)$ . In the

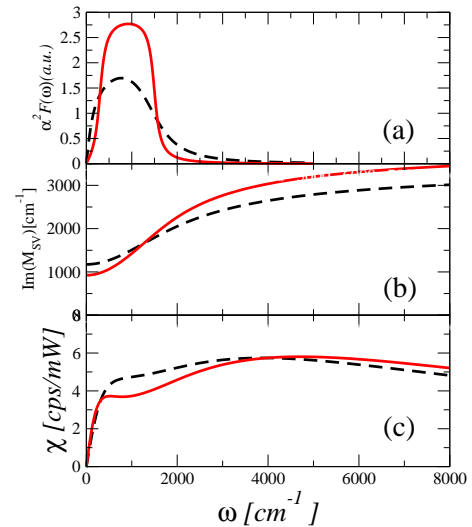


FIG. 7: (a) Glue functions for two CMs having the same dynamical range between  $\omega_1 = 330 \text{ cm}^{-1}$  and  $\omega_2 = 1500 \text{ cm}^{-1}$ , but different diffusive-propagating crossover scale:  $\bar{\Omega} = 200 \text{ cm}^{-1}$  for the more propagating mode (solid red curve),  $\bar{\Omega} = 1000 \text{ cm}^{-1}$  for the more diffusive mode (dashed black curve). (b) Imaginary part of the memory function (scattering time) corresponding to the two glue functions in (a). (c) Raman response obtained for the two glue functions in (a) with  $g^2 = 0.5$ .

forthcoming discussion it is important to observe that the overall behavior of the Raman response is qualitatively understood by inspecting the behavior of the frequency dependent inverse scattering time  $1/\tau(\omega) = ImM(\omega)$ , since the mass corrections associated to  $ReM(\omega)$  do not introduce significant features.

A nearly constant  $1/\tau$  produces a Drude-like peak at frequency  $\omega \approx 1/\tau$ . A nearly linear  $1/\tau$  produces instead a flattish (i.e., marginal-Fermi-liquid-like) response. Now, we see that a diffusive CM (large  $\bar{\Omega}$ ) is characterized by a broadly peaked glue function [see black dashed line in Fig. 7(a)]. This, in turn, yields a  $1/\tau$  which smoothly interpolates between the low-frequency value ( $1/\tau_0$ ) and the high-frequency value ( $1/\tau_{\infty} > 1/\tau_0$ ) [see black dashed line in Fig. 7(b)]. The Raman spectrum is correspondingly characterized by a hump+hump overall shape which results from the overlap of two Drude peaks roughly centered at  $1/\tau_0$  and  $1/\tau_{\infty}$  [see black dashed line in Fig. 7(c)]. This corresponds to the  $B_{1g}$  spectra experimentally observed in LSCO. If the CM has a marked propagating character (small  $\bar{\Omega}$ ), the corresponding glue function has instead the shape of a rounded box function [see red solid line in Fig. 7(a)]. This, in turn, implies a broad linear regime in  $1/\tau$  and a wider separation between  $1/\tau_0$  and  $1/\tau_{\infty}$ . The corresponding Raman spectra has the step+hump form [see red solid line in Fig. 7(c)], similar to the  $B_{2g}$  spectra experimentally observed in LSCO.

### Appendix C: Relaxing the selection rules

The channel-dependent selection rule for the Raman spectra was obtained under two main assumptions: (1) the CMs are peaked at finite wavevectors  $\mathbf{q}_\lambda$  and (2) the factorized fermion loops are dominated by QPs at the hot spots. The second assumption is asymptotically valid at low frequency, but is gradually violated at higher frequency. This means that at sufficiently large  $\omega$  both CMs contribute to Raman spectra, regardless of the symmetry. This is expected on theoretical grounds and indeed observed experimentally: the  $B_{1g}$  and  $B_{2g}$  spectra of LSCO have similar shapes at high frequency, indicating that channel-dependent selection rules are not at work there.

However, the analytical evaluation of the fermion loops beyond the hot-spot contribution is not viable and the numerical evaluation is both demanding and not transparent. Thus, in our calculation we adopted an alternative phenomenological description, writing the memory function as  $M(\omega) = M_a(\omega) + s(\omega)M_f(\omega)$ , where  $M_a(\omega)$  is the memory function associated with the CM allowed

by the selection rule and  $M_f(\omega)$  is the memory function associated with the CM forbidden by the selection rule. The switch function

$$s(\omega) = \frac{1}{2} \left[ 1 + \tanh \left( \frac{\omega - \omega_f}{\beta_f} \right) \right]$$

gradually includes the contribution of the forbidden CM at a frequency  $\omega \approx \omega_f$ . The rapidity of the inclusion is controlled by the parameter  $\beta_f$ . Typical values in our fits are  $\omega_f \sim 10^3 \text{ cm}^{-1}$  and  $\beta_f \sim 5 \times 10^2 \text{ cm}^{-1}$ , roughly common to both charge and spin modes. We point out that our phenomenological procedure is not fully causal (i.e.,  $ReM$  and  $ImM$  are no longer related by Kramers-Kronig transformations). However, since a constant  $s(\omega)$  would restore causality, a sufficiently gradual inclusion of the forbidden CM does not introduce significant drawbacks. Below the frequency  $\omega_f$ , the spectra in the  $B_{1g}$  and  $B_{2g}$  symmetries are markedly different, whereas above  $\omega_f$  they gradually become similar in shape.

- 
- <sup>1</sup> Anderson, P. W. Is there glue in cuprate superconductors? *Science* **316**, 1705-1707 (2007).
- <sup>2</sup> Anderson, P.W. The resonating valence bond state in  $\text{La}_2\text{CuO}_4$  and superconductivity. *Science* **235**, 1196-1198 (1987).
- <sup>3</sup> Lee, P. A., Nagaosa, N. & Wen, X. G. Doping a Mott insulator: Physics of high-temperature superconductivity. *Rev. Mod. Phys.* **78**, 1785 (2006).
- <sup>4</sup> Maier T. A., Poilblanc D., Scalapino D. J., Dynamics of the Pairing Interaction in the Hubbard and t-J Models of High-Temperature Superconductors, *Phys. Rev. Lett.* **100**, 237001 (2008) and references therein.
- <sup>5</sup> Hanke W., Kiesel M. L., Aichhorn M., Brehm S., and Arrigoni E., The 3-band Hubbard-model versus the 1-band model for the high- $T_c$  cuprates: Pairing dynamics, superconductivity and the ground-state phase diagram, *Eur. Phys. J. Special Topics* **188**, 15 (2010) and references therein.
- <sup>6</sup> Abanov Ar., Chubukov A., & Schmalian J., Quantum-critical theory of the spin-fermion model and its application to cuprates: normal state analysis, *Adv. Phys.* **52**, 119 (2003), and references therein.
- <sup>7</sup> Castellani C., Di Castro C., & Grilli M., Singular quasi-particle scattering in the proximity of charge instabilities, *Phys. Rev. Lett.* **75**, 4650 (1995).
- <sup>8</sup> Varma C. M., Theory of Copper-Oxide Metals, *Phys. Rev. Lett.* **75**, 898 (1995).
- <sup>9</sup> Varma C. M., Non-Fermi-liquid states and pairing instability of a general model of copper oxide metals, *Phys. Rev. B.* **55**, 14554 (1997), and references therein.
- <sup>10</sup> Tallon J. L., & Loram J.W., The doping dependence of  $T^*$  - What is the real high- $T_c$  phase diagram?, *Physica C* **349**, 53 (2001).
- <sup>11</sup> Castellani C., Di Castro C., & Grilli M., *J. of Phys. and Chem. of Sol.* **59**, 1694 (1998).
- <sup>12</sup> Benfatto L., Caprara S., & Di Castro C., Gap and pseudo-gap evolution within the charge-ordering scenario for superconducting cuprates, *Eur. Phys. J. B* **17**, 95-102 (2000).
- <sup>13</sup> Chakravarty S., Laughlin R. B., Morr D. K., & Nayak C., Hidden order in the cuprates, *Phys. Rev. B* **63**, 094503 (2001).
- <sup>14</sup> Metzner W., Rohe D., & Andergassen S., Soft Fermi Surfaces and Breakdown of Fermi-Liquid Behaviour, *Phys. Rev. Lett.* **91**, 066402 (2003)
- <sup>15</sup> Shastry S. & Shraiman B., Theory of Raman scattering in Mott-Hubbard systems, *Phys. Rev. Lett.* **103**, 1078 (1990).
- <sup>16</sup> Devereaux, T.P., & Hackl R., Inelastic light scattering from correlated electrons, *Rev. Mod. Phys.* **79**, 175 (2007).
- <sup>17</sup> Millis A. J., Monien H., & Pines D., Phenomenological model of nuclear relaxation in the normal state of  $\text{YBa}_2\text{Cu}_3\text{O}_7$ , *Phys. Rev. B* **42**, 167 (1990).
- <sup>18</sup> Mahan G. D., *Many-Particle Physics*, Kluwer Academic/Plenum Publisher (New York, Boston, Dordrecht, London, Moscow, Ch. 8).
- <sup>19</sup> Götze W. & Wölfle P., Homogeneous dynamical conductivity of symple metals, *Phys. Rev. B* **6**, 1226 (1972).
- <sup>20</sup> Varma C. M., Phenomenological constraints on theories for high temperature superconductivity, *Int. J. Mod. Phys. B* **3**, 2083 (1989).
- <sup>21</sup> Varma C. M., Littlewood P. B., Abrahams E., & Ruckenstein, Phenomenology of the normal state of Cu-O high-temperature superconductors, *Phys. Rev. Lett.* **63**, 1996 (1989).
- <sup>22</sup> Norman M. R. & Chubukov A. V., High-frequency behaviour of the infrared conductivity of cuprates, *Phys. Rev. B* **73**, 140501(R) (2006).
- <sup>23</sup> Wakimoto S., Yamada K., Tranquada J. M., Frost C. D., Birgeneau R. J., & Zhang H., Disappearance of Antiferromagnetic Spin Excitations in Overdoped  $\text{La}_{2-x}\text{Sr}_x\text{CuO}_4$ , *Phys. Rev. Lett.* **98**, 247003 (2007).
- <sup>24</sup> Wakimoto S., Zhang H., Yamada K., Swainson I., Kim Hyun kyung, & Birgeneau R. J., Direct Relation between

- the Low-Energy Spin Excitations and Superconductivity of Overdoped High-Tc Superconductors, *Phys. Rev. Lett.* **92**, 217004 (2004).
- <sup>25</sup> Becca F., Tarquini M., Grilli M., & Di Castro C., Charge-Density-Waves and superconductivity as an alternative to phase separation in the infinite-U Hubbard-Holstein model, *Phys. Rev. B* **54**, 12443 (1996).
- <sup>26</sup> Castellani C., Di Castro C., & Grilli M., Non-Fermi-liquid behaviour and *d*-wave superconductivity near the charge-density-wave quantum critical point, *Zeit. für Phys. B* **103**, 137 (1997)
- <sup>27</sup> Muschler B., Prestel W., Schachinger E., Carbotte J. P., Hackl R., Ono S., & Ando Y., An electron-boson glue function derived from electronic Raman scattering, *J. Phys.: Condens. Matter* **22**, 375702 (2010).
- <sup>28</sup> Bogdanov P. V., Lanzara A., Kellar S. A., Zhou X. J., Lu E. D., Zheng W. J., Gu G., Shimoyama J.-I., Kishio K., Ikeda H., Yoshizaki R., Hussain Z., & Shen Z. X., Evidence for an energy scale for quasiparticle dispersion in Bi<sub>2</sub>Sr<sub>2</sub>CaCu<sub>2</sub>O<sub>8</sub>, *Phys. Rev. Lett.* **85**, 2581 (2000).
- <sup>29</sup> Garcia D.R. & Lanzara A., Through a Lattice Darkly Shedding Light on Electron-Phonon Coupling in the High Tc Cuprates, *Adv. in Cond. Mat. Physics, Special Issue "Phonons and Electron Correlations in High-Temperature and Other Novel Superconductors"*, Volume 2010 (2010), Article ID 807412, Guest Editors: Sasha Alexandrov, Carlo Di Castro, Igor Mazin, & Dragan Mihailovic, and references therein.
- <sup>30</sup> Hashimoto M., He R.-H., Tanaka K., Testaud J.-P., Meevasana W., Moore R. G., Lu D., Yao H., Yoshida Y., Eisaki H., Devereaux T. P., Hussain Z., & Shen Zhi-Xun, Particle-hole symmetry breaking in the pseudogap state of Bi<sub>2</sub>201, *Nat. Phys.* **6**, 414-418 (2010).
- <sup>31</sup> Howald C., Eisaki H., Kaneko N., Greven M., & Kapitulnik A., Periodic density-of-states modulations in superconducting Bi<sub>2</sub>Sr<sub>2</sub>CaCu<sub>2</sub>O<sub>8+δ</sub>, *Phys. Rev. B* **67**, 014533 (2003).
- <sup>32</sup> Hanaguri T., Lupien C., Kohsaka Y., Lee D.-H., Azuma M., Takano M., Takagi H., & Davis J. C., A 'checkerboard' electronic crystal state in lightly hole-doped Ca<sub>2-x</sub>Na<sub>x</sub>CuO<sub>2</sub>Cl<sub>2</sub>, *Nature* **430**, 1001 (2004).
- <sup>33</sup> Kohsaka Y., Taylor C., Wahl P., Schmidt A., Lee Jhin-hwan, Fujita K., Alldredge J. W., McElroy K., Lee Jinho, Eisaki H., Uchida S., Lee D.-H. & Davis J. C., How Cooper pairs vanish approaching the Mott insulator in Bi<sub>2</sub>Sr<sub>2</sub>CaCu<sub>2</sub>O<sub>8+δ</sub>. *Nature* **454**, 1072-1078 (2008).
- <sup>34</sup> Lee Jinho, Fujita K., McElroy K., Slezak J. A., Wang M., Aiura Y., Bando H., Ishikado M., Masui T., Zhu J.-X., Balatsky A. V., Eisaki H., Uchida S. & Davis J. C., Interplay of electron-lattice interactions and superconductivity in Bi<sub>2</sub>Sr<sub>2</sub>CaCu<sub>2</sub>O<sub>8+δ</sub>, *Nature* **442**, 546 (2006).
- <sup>35</sup> Hofer J., Conder K., Sasagawa T., Zhao Guo-meng, Willemin M., Keller H., & Kishio K., Oxygen-Isotope Effect on the In-Plane Penetration Depth in Underdoped La<sub>2-x</sub>Sr<sub>x</sub>CuO<sub>4</sub> Single Crystals, *Phys. Rev. Lett.* **84**, 4192 (2000).
- <sup>36</sup> Rubio Temprano D., Mesot J., Janssen S., Conder K., Furrer A., Mutka H., Müller K. A., *Phys. Rev. Lett.* **84**, 1990 (2000).
- <sup>37</sup> Suryadijaya, Sasagawa T., Takagi H., Oxygen isotope effect on charge/spin stripe in La<sub>1.8-x</sub>Eu<sub>0.2</sub>Sr<sub>x</sub>CuO<sub>4</sub>. *Physica C* **426-431**, 402 (2005).
- <sup>38</sup> Andergassen S., Caprara S., Di Castro C., & Grilli M., Anomalous Isotopic Effect Near the Charge-Ordering Quantum Criticality. *Phys. Rev. Lett.* **87**, 056401 (2001).
- <sup>39</sup> Yang J., Hwang J., Schachinger E., Carbotte J. P., Lobo R. P. S. M., Colson D., Forget A., and Timusk T., Exchange Boson Dynamics in Cuprates: Optical Conductivity of HgBa<sub>2</sub>CuO<sub>4+δ</sub>, *Phys. Rev. Lett.* **102**, 027003 (2009).
- <sup>40</sup> van Heumen E., Muhlethaler E., Kuzmenko A. B., Eisaki H., Meevasana W., Greven M., & van der Marel D., Optical determination of the relation between the electron-boson coupling function and the critical temperature in high T<sub>c</sub> cuprates, *Phys. Rev. B* **79**, 184512 (2009).
- <sup>41</sup> Schachinger E. and Carbotte J.P., Finite band inversion of angular-resolved photoemission in Bi<sub>2</sub>Sr<sub>2</sub>CaCu<sub>2</sub>O<sub>8+δ</sub> and comparison with optics, *Phys. Rev. B* **77**, 094524 (2008)
- <sup>42</sup> Jin Mo Bok, Jae Hyun Yun, Han-Yong Choi, Wentao Zhang, Zhou X. J., & Varma C. M., Momentum dependence of the single-particle self-energy and fluctuation spectrum of slightly underdoped Bi<sub>2</sub>Sr<sub>2</sub>CaCu<sub>2</sub>O<sub>8+δ</sub> from high-resolution laser angle-resolved photoemission, *Phys. Rev. B* **81**, 174516 (2010).
- <sup>43</sup> Tassini L., Venturini F., Zhang Q.-M., Hackl R., Kikugawa N., Fujita T., Dynamical Properties of Charged Stripes in La<sub>2-x</sub>Sr<sub>x</sub>CuO<sub>4</sub>, *Phys. Rev. Lett.* **95**, 117002 (2005).
- <sup>44</sup> Caprara S., Di Castro C., Grilli M., & Suppa D., Charge-Fluctuation Contribution to the Raman Response in Superconducting Cuprates, *Phys. Rev. Lett.* **95**, 117004 (2005).
- <sup>45</sup> Basov D. N. & Timusk T., Electrodynamics of high-T<sub>c</sub> superconductors, *Rev. Mod. Phys.* **77**, 721 (2005)
- <sup>46</sup> Puchkov A. V., Basov D. N., & Timusk T., Pseudogap state in high-T<sub>c</sub> superconductors: an infrared study, *J. Phys.: Condens. Matter* **8**, 10049 (1999).
- <sup>47</sup> Hwang J., Timusk T., & Gu G. D., High-transition-temperature superconductivity in the absence of the magnetic-resonance mode, *Nature* **427**, 714 (2004).
- <sup>48</sup> Dahm T., Hinkov V., Borisenko S. V., Kordyuk A. A., Zabolotny V. B., Fink J., Büchner B., Scalapino D. J., Hanke W. and Keimer B., Strength of the spin-fluctuation-mediated pairing interaction in a high-temperature superconductor, *Nat. Phys.* **5**, 217 (2009).
- <sup>49</sup> Muschler B., Prestel W., Tassini, L., Hackl, R., Lambacher, M., Erb, A., Komiya, Seiki, Ando, Yoichi, Peets, D.C., Hardy, W.N., Liang, R., and Bonn, D.A., Electron interactions and charge ordering in CuO<sub>2</sub> compounds *Eur. Phys. J. Special Topics* **188**, 131 (2010)
- <sup>50</sup> Lambacher, M., Helm, T., Kartsovnik, M., Erb, A., Advances in single crystal growth and annealing treatment of electron-doped HTSC *Eur. Phys. J. Special Topics* **188**, 61 (2010)